# Delayed hydride cracking of Zr-2.5%Nb pressure tube material due to partially constrained precipitates

Murty, T. Narayana; Singh, R. N.; Ståhle, P.

*Published in:*
Journal of Nuclear Materials

*DOI:*
10.1016/j.jnucmat.2018.10.040

2019

*Document Version:*
Publisher's PDF, also known as Version of record

Journal of Nuclear Materials 513 (2019) 129–142

Contents lists available at ScienceDirect

Journal of Nuclear Materials

journal homepage: www.elsevier.com/locate/jnucmat

# Delayed hydride cracking of Zr-2.5%Nb pressure tube material due to partially constrained precipitates

T. Narayana Murty [a, b], R.N. Singh [a, b, *], P. Ståhle [c]

[a] Mechanical Metallurgy Division, Bhabha Atomic Research Centre, Mumbai, 400085, India
[b] Homi Bhabha National Institute, Anushaktinagar, Mumbai, 400094, India
[c] Division of Solid Mechanics, Lund University, Lund, 221 00, Sweden

## GRAPHICAL ABSTRACT

In Fig. 1(a) and (b) plot of *KJ* as a function of aspect ratio of oxide nodules for different depths using unirradiated and irradiated material properties is shown. Also depicted in this figure are the reported values of threshold stress intensity factors above which crack growth by Delayed Hydride Cracking is possible. It is evident form figures that in cases of unirradiated material, oxide nodules having aspect ratios less than two and depths more than 350 μm can initiate DHC whereas nodules having aspect ratios less than 2.5 and depths more than 200 μm can initiate DHC in irradiated material.

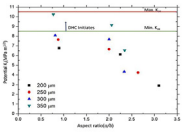

Figure1(a) *KJ* for un irradiated material

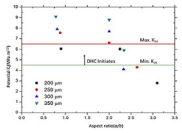

## ARTICLE INFO

*Article history:*
Received 29 June 2018
Received in revised form
16 October 2018
Accepted 24 October 2018
Available online 1 November 2018

*Keywords:*
Zr-2.5%Nb alloy
Hydride blister
Oxide nodule
Finite element method
Stress field
Delayed hydride cracking

## ABSTRACT

Formation of partially constrained precipitates such as hydride blisters and oxide nodules have been reported on surfaces of Zr-alloy components of pressurised heavy water reactors and is associated with a large increase in volume. Such a change in volume imposes large stresses in the material surrounding the precipitate and may facilitate stable crack growth through delayed hydride cracking. In this work, the stress field of the partially constrained precipitates with different depth and aspect ratio has been computed using a finite element method. The computed stress field is used to predict the region in the matrix in which radial hydride is likely to form and fracture, by taking into consideration grain-size, texture and multi-axial state of stress. For a hypothetical crack just below the precipitate, stress intensity factors are estimated using material properties for both unirradiated and irradiated pressure tube materials. The results are compared with the threshold stress intensity factors required for crack growth due to delayed hydride cracking.



## 1. Introduction

Formation of precipitates in the material and their interaction with the matrix material has always been a fascinating topic for

* Corresponding author. Mechanical Metallurgy Division, Bhabha Atomic Research Centre, Mumbai, 400085, India.
*E-mail address:* rnsingh@barc.gov.in (R.N. Singh).

https://doi.org/10.1016/j.jnucmat.2018.10.040
0022-3115/

materials scientists since early days [1,2]. Majority of these investigations are aimed at developing better understanding of fully constrained precipitates. However, if the localised precipitation takes place at or near the surface and is associated with large transformation strain, the boundary of the transformed region will behave as a crack through which a wedge is being driven. Formation of hydride blisters [3–5] and oxide nodules [6–9] in the Zr-alloy components [10–12] are examples of such localised precipitations. The stress free volume change associated with hydride formation in Zr-alloys is reported to be 17–20% depending on the temperature of transformation [13] and the volume change associated with tetragonal oxide formation in Zr-alloys is 56% [14].

The pressure tubes of pressurised heavy water reactors (PHWR), which are made of a Zr-2.5%Nb alloy, act as a boundary for a hot pressurised coolant and its integrity during reactor operation is very important as they are the first containment in the nuclear reactor safety systems. The pressure tubes have been reported to fail due to the formation of hydride blisters on the tube surfaces [3]. Cracks were initiated in the hydride blisters due to the stress field generated during the formation of the hydride blister and hoop stress and residual stresses (if any) in the pressure tube. These cracks grew into the matrix material and propagated through thickness by the delayed hydride cracking (DHC) mechanism [15,16]. Similarly, formation of the oxide nodules can also induce stresses in the matrix material and may lead to stable crack growth by the DHC phenomenon. It is to be noted that there are differences in the mechanism of nucleation and growth of hydride blisters and oxide nodules, the species causing their formation (hydrogen for hydride blisters and oxygen for oxide nodules) role of the temperature gradient during hydride blister formation and hydrogen concentration gradient associated with hydride blisters. However, both hydride blisters and oxide nodules forms on the surface and reason of stress field generation in the matrix is large transformation strains associated with their formation. Thus, mention or comparisons of the hydride blister and oxide nodules in the present manuscript is due to their mechanistic similarity. A good amount of work has been done to understand the formation of hydride blisters and their role in cracking of Zr-2.5%Nb pressure tubes [17]. Oxide nodules are also expected to critically affect the integrity of the pressure tubes as the volumetric expansion during their formation is three times that of the hydride blister. Their role in the integrity of the tubes is technologically very important and not well understood. Therefore, a stress field computation is necessary to assess the integrity of the internally pressurised pressure tube.

Sawatzky [4], from his studies estimated the time required to grow a blister to a particular size. From his studies, it can be concluded that blister growth is a gradual and multi physics coupled phenomenon as it involves precipitation kinetics, phase transformation, thermodynamics, solid mechanics and fracture mechanics. Kim and Vanderglas [18] and Vanderglass [19] computed the stress field assuming that the blister has grown in a single step. Later Singh et al. [20] computed the stress field assuming that predefined size of blister has grown in multiple steps. Reheman et al. [21] simulated the growth of an expanding precipitate by using a phase field model considering coupled diffusion, precipitate formation and elastic-plastic deformation. However, they assumed that the matrix and the precipitate have the same mechanical properties. The stress field due to an oxide nodule is not reported till now. All the models and experiments [22–26], which attempted to explain the formation of radial hydrides did not consider the combined effect of the grain size, texture and state of stress in the material.

The objective of this work is to compute the stress field of the partially constrained oxide nodule using finite element calculations and to predict the region of the radial hydride formation in the matrix by nucleation kinetics model using the computed stress field. In the present study, the stress fields of oxide nodules are computed by sequentially recalculating the mechanical state and growth in several steps. A new model to predict the radial hydride formation by taking into consideration the combined effect of grain size, texture and state of stress in material is proposed in this study. The computed stress is used to predict the size of radial hydrides that are likely to fracture. Finally, a predefined crack is introduced in the matrix at the deepest point of the nodule to find potential stress intensity factors. Calculated stress intensity factors are used to predict the size of the nodule that will initiate stable crack growth through the DHC mechanism.

## 2. Stress field calculations

### 2.1. The finite element model

The geometry of the three-dimensional model for the present study is obtained from the pressure tube of the PHWRs. The thickness of the pressure tube (PT) of a 220 MW electric power is 3.5 mm and inner radius of the tube is 42 mm [27]. A single nodule is assumed to be formed on the outer surface of the pressure tube. Typical size of the oxide nodule is about few tens microns to few hundred microns. As the size of nodule is very small compared to the pressure tube dimensions, a small section of the pressure tube is considered for the analysis. The curvature of tube is neglected as size of the nodule is very small compared to dimensions of pressure tube. The planar view of the oxide nodule on the PT surface is assumed to be circular. Fig. 1 describes the three-dimensional finite element model used for the analysis. The size of the model is chosen in such a way that the stress field generated due to the formation of oxide nodule will not be effected by the boundary conditions and free surfaces. The global Cartesian coordinate system $x$, $y$, $z$ is shown in Fig. 1. The global $x$, $y$, $z$ coordinate axes coincides with the axial, radial, tangential directions of the pressure tube, respectively.

Maximum internal pressure acting on the inside surface of the pressure tube is 10 MPa during reactor operation [27]. This pressure loading generates hoop, longitudinal, and radial stresses in the pressure tube. According the ASME section 8, if r/t value of tube is greater than 10, shell can be considered as thin. In the pressure tube case r/t value is about 12 and therefore, it is not expected to affect the computed stress field. Therefore, at a large distance from the oxide nodule and the crack, the hoop stress $pd/2t$ and longitudinal stress $pd/4t$ are calculated, where $p$ is the difference between the

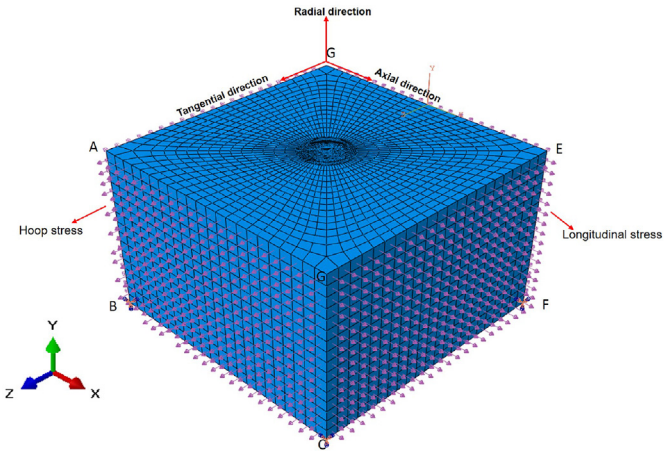


**Fig. 1.** Finite element model with loading and boundary conditions.

internal and external pressures, $t$ is the thickness of the pressure tube and $d$ is the internal diameter of the pressure tube. Radial stresses are neglected as they are of the order of $p$ which is considered to be small compared to the other two stresses. Fig. 1 shows the loading for the finite element model having the corners A-H. The hoop stress $pd/2t$ is applied to the surfaces A-D and E-H along the $z$ direction, and the longitudinal stress $pd/4t$ is applied to the surfaces C-F and A, B, G and H along the $x$ direction.

The body occupies the region $|x| \le L/2,\ -t \le y \le 0,\ |z| \le H/2$, and the nodule is forced to initiate at $x = y = z = 0$. Here $L$ represents total length along axial direction, $t$ represents wall thickness of the tube and $H$ represents the total length along hoop direction. The boundary conditions are

$$\begin{aligned}
&\sigma_{xx} = \frac{pd}{4t},\ \sigma_{xy} = \sigma_{xz} = 0,\ \text{on}\ \left|x\right| = \frac{L}{2},\ -t \le y \le 0,\ \left|z\right| \le \frac{H}{2},\\
&\sigma_{yy} = \sigma_{xy} = \sigma_{yz} = 0,\ \text{on}\ \left|x\right| \le \frac{L}{2},\ y = -t \text{ and } y = 0,\ \left|z\right| \le \frac{H}{2},\\
&\sigma_{zz} = \frac{pd}{2t},\ \sigma_{xz} = \sigma_{yz} = 0,\ \text{on}\ \left|x\right| \le \frac{L}{2},\ -t \le y \le 0,\ \left|z\right| = \frac{H}{2}.
\end{aligned} \tag{1}$$

To prevent the rigid body motion to have free deformation of the model, three nodes in a plane i.e. B, C, F are selected as shown in Fig. 1. Node B is fully constrained, $u = v = w = 0$, where $u$, $v$ and $w$ are the displacements in the $x$, $y$ and $z$ directions, respectively. Node C is constrained in two directions that are perpendicular to vector BC, i.e., $v = w = 0$, and node F is restricted to move in direction that is perpendicular to vectors BC and CF, i.e., $v = 0$.

Finite element meshing of the model is shown in Fig. 2. The model is partitioned into three regions. They are the initial nuclei of the oxide formed and the region, which encloses the final size of oxide nodule formed and the region in which stress decays to the far field stress. In order to study the stress at the material discontinuities very fine mesh is used in the region 1 and region 2, which is shown at the corner of Fig. 2. The size of the element used in the region 1 and 2 is 5 $\mu$m−10 $\mu$m and size of the elements used in the region 3 is 100 $\mu$m. Isotropic material properties are considered in the present analysis. The material properties are those obtained at the temperature of 300 °C. The material models for the metal and the metal oxide are assumed to be elastic-plastic isotropic with a von Mises yield criteria and an associated flow rule.

The elastic-plastic behaviour of Zr-2.5%Nb reported in literature is used in the analysis [28]. The elastic modulus is 90 GPa and Poisson's ratio is taken to be 0.4. The 0.2% plastic strain yield stress is 463.2 MPa and the hardening rate is initially 15.8 GPa and at 3.19% plastic strain has decreased to 1.43 GPa. For higher plastic strains the zirconium alloy is assumed to be perfectly plastic. Thus, the ultimate von Mises effective stress is 602 MPa reached at 3.19% plastic strain. The changes of the hardening rate is broken up into eight piecewise linear intervals closely following the experimental results of [28].

The elastic modulus of the nodule material, $ZrO_2$, is taken to be 200 GPa and Poisson's ratio is taken to be 0.3. The oxide is assumed to be perfectly plastic with the yield stress put to be 700 MPa [30]. Elastic-plastic finite element analysis is performed using the commercial software package Abaqus [29]. Three-dimensional continuum elements (C3D8R) with linear interpolation for displacements between nodes are used. Large scale plastic deformation is expected in the Zr-2.5%Nb matrix material due to the large expansion of the hard oxide nodule during its formation.

### 2.2. Methodology

Classical analytical solution of the stress field for an ellipsoidal geometry precipitate, which is completely embedded in an elastic material was given by Eshelby [1]. In this work the stress field was calculated by cutting the precipitate material from the matrix material, imposing the misfit strain on the precipitate and finally welding precipitate to the matrix material. No analytical solutions are, to the authors' knowledge, given for the semi constrained precipitates. However, the finite element method can be used to find the stress field numerically. Kim and Vanderglas [18], and Vanderglas [19] computed the stress field using initial strain method using FEM. They computed the stress field for the hydride blister case assuming that the precipitate has a fixed size from the beginning of hydride precipitation rather than growing from infinitesimal size to a certain size, which is indeed the case. The expansion due to precipitation was modelled by imposing the initial strain in the predefined hydride blister region. In the hydride blister case, the hydrogen concentration in the precipitate varies along the thickness of the precipitate. So, they assumed that initial strain imposed is proportional to local hydrogen concentration.

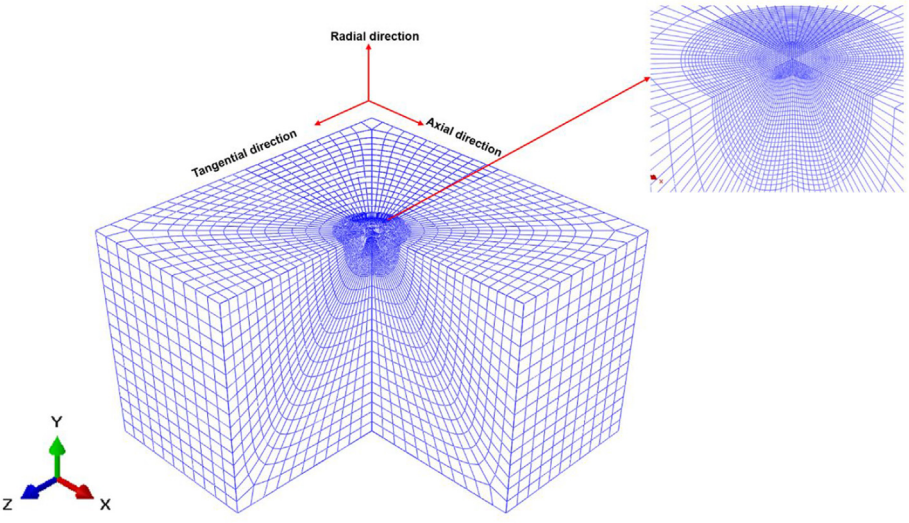


**Fig. 2.** Meshing of the model.

Therefore, they imposed different strain functions in the precipitate region. Singh et al. [31] cut the precipitate from the matrix material. They had calculated the unconstrained displacement from the total displacement by partitioning the misfit strain between matrix and blister. Finally, they imposed unconstrained displacement on the imaginary notch created in the matrix by removing precipitate from the matrix and they solved it numerically by using FEM method. None of the methods mentioned above consider the growth of the precipitate. Singh et al. [20] divided the predefined precipitate region into multiple layers. They had imposed the strain on each layer sequentially to final layer of the precipitate. Ståhle et al. [32] gave an analytical solution for the completely embedded precipitate, which grows from the infinitesimally small size to final size in a perfectly elastic plastic material. In their analysis, they used uniform isotropic expansion of the precipitate. A similar analysis was performed.

As in Ref. [32], also in the present analysis, a predefined region is not demarcated from the matrix material rather growth of the oxide nodule is considered. The methodology to fulfil this objective is described below.

A very small region in the matrix of the length $a$ and 50 $\mu$m depth is partitioned at the centre of the model. The length $a$ is varied to get the different sizes of the final oxide nodules. This region is transformed to oxide nodule in the initial step. The oxide nodule, which is formed from the matrix material swells because of the change of the crystal structure. Swelling of the new material will be resisted by the matrix. This swelling of oxide nodule is simulated by imposing an initial strain, which is typically used in the thermal analysis [33]. During transformation, the material properties of the matrix material are linearly interpolated to those of the precipitate material. Due to this initial transformation of the precipitate, stresses and strains will be generated in the matrix, which is expected to drive the oxide nodule growth in the subsequent steps. The volumetric strain, which is the sum of normal strain components, i.e., $\varepsilon_v = \varepsilon_{xx} + \varepsilon_{yy} + \varepsilon_{zz}$ is calculated in the matrix material. Elements in which volumetric strain is greater than 1% are transformed to obtain the material properties and expansion of the oxide. The transformed properties are implemented in the following time increment. Again, due to transformation of these elements, stresses and strains will be generated in the remaining matrix. The above procedure is repeated to simulate the growth of the precipitate.

The volume change during the transformation of zirconium to $ZrO_2$ is given by the Pilling-Bedworth ($R_{PB}$) ratio [14]. The $R_{PB}$ value corresponding to the formation of $ZrO_2$ from zirconium is 1.56. The expansion of $ZrO_2$ is assumed to be isotropic. The stress free swelling of the oxide nodule is defined as follows,

$$\varepsilon^s_{xx} = \varepsilon^s_{yy} = \varepsilon^s_{zz} = \sqrt[3]{R_{PB}} - 1 \tag{2}$$

### 2.3. The FEM model

Different initial sizes of initial nuclei are demarcated from the matrix material to get the different sizes of the final oxide nodule. In the present analysis three different sizes of initial nuclei of depth $b = 50\mu$m and diameters $a = 100\mu$m, $250\mu$m and $500\mu$m were considered. Oxide nodule was grown by incorporating transformed matrix material in the initial nuclei in multiple steps. The methodology described section 2.2 is used to add transformed matrix material to the nodule.

The dimensions and axes used for plotting the results are schematically shown in Fig. 3. The stresses in the matrix are plotted along the vertical axis normalised with respect to the depth $b$ of the nodule. The aspect ratio ($AR$) of the nodule is defined as $a/b$.

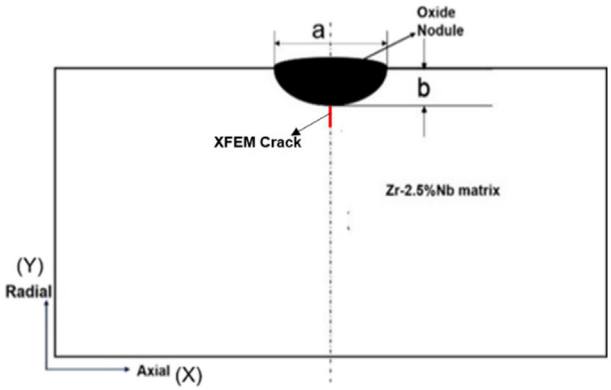


**Fig. 3.** Illustration of dimensions of oxide nodule along with XFEM crack and axes used for plotting the results.

The contour plot of stresses for nodules that were grown to the final aspect ratio 3 and 0.78 are presented in Figs. 4 and 5, respectively. For a better demonstration of the results contour plots are presented in axial radial plane, which cuts the nodule into two halves. The state of stress is very complex as evident from Figs. 4 and 5. High tensile stresses are generated in the upper layers of the oxide nodule, due to these stresses, cracks may appear in the top layers of the nodules. The tensile stresses are also generated in

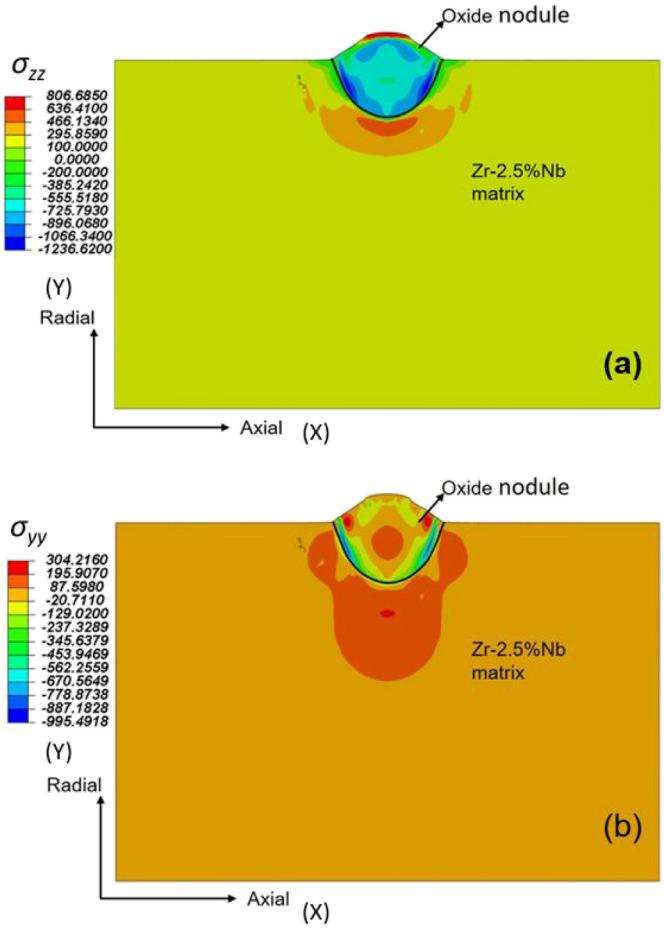


**Fig. 4.** Contour plots of (a) $\sigma_{zz}$, (b) $\sigma_{yy}$ in MPa for the final nodule size 275$\mu$m × 350$\mu$m.

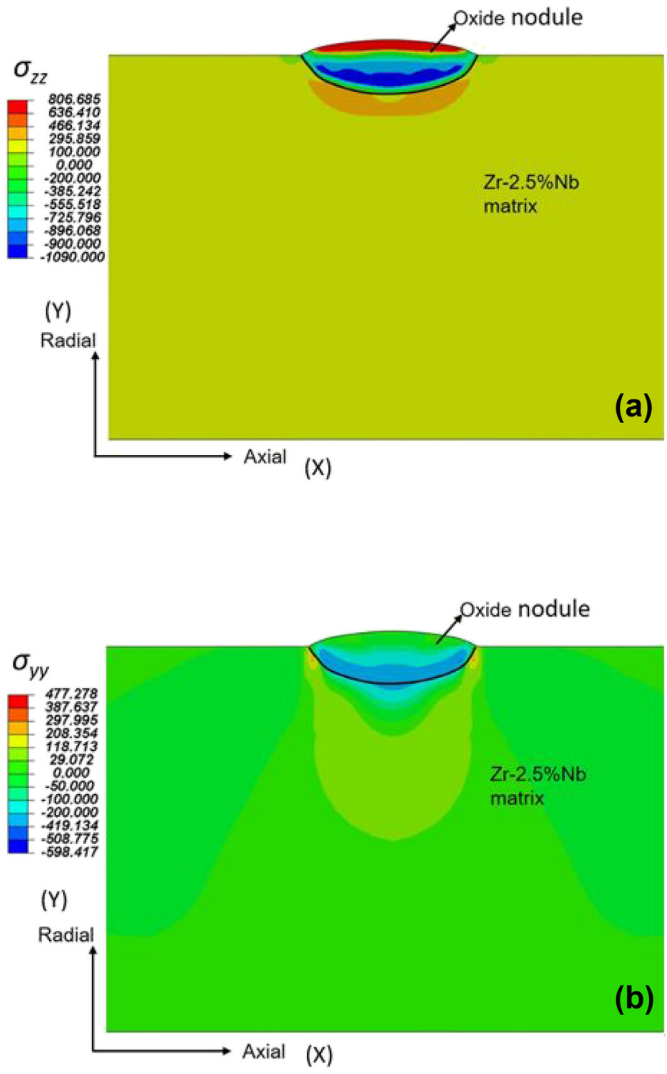


**Fig. 5.** Contour plots of (a) $\sigma_{zz}$, (b) $\sigma_{yy}$ in MPa for the final nodule size of 620$\mu$m$\times$ 200$\mu$m.

the matrix below the nodule, which was observed to decay to far field stresses as one move away from the interface of oxide nodule.

These results show that the stresses in the matrix are decreasing with increase in aspect ratio of the nodule. The variation of $\sigma_{xx}$ and $\sigma_{zz}$ are similar due to isotropic expansion of the oxide nodule. The difference in the absolute values of these stress values is due to the difference in the externally applied longitudinal and hoop stress. The distribution of $\sigma_{yy}$ is different from the other two stresses, this is due to the free surface, which imposes partial constraint to the growth of the oxide nodule. The stresses in the circumferential $\sigma_{zz}$ direction are plotted in Fig. 6.

Fig. 6 suggest that the pronounced effect of oxide nodule is up to the distance of about four times the depth of the nodule in the matrix material. The stresses also depend on the initial nuclei size assumed. The peak stress values are shifting away from the interface with increase in the aspect ratio of the oxide nodule. The peak stresses are exceeding the yield strength of the material in case of nodules having aspect ratios less than two. These stresses are reducing drastically for nodules having aspect ratio more than two.

The stresses in the radial direction ($\sigma_{yy}$) are plotted in Fig. 7. For all examined nodules the $\sigma_{yy}$ stresses in the matrix are numerically below the yield stress of the nodule. The stresses are compressive near the matrix nodule interface for nodules having an aspect ratio larger than two.

### 2.4. Validation of FEM computation using bulge height

It is difficult to experimentally verify the numerical results because of the small size of the oxide nodule and conventional residual stress measurement techniques cannot be applied due to the small size of the nodule. The protrusion of the nodule from the free surface is called bulging height. The only measurable quantity available from the experiments is the bulging height of the nodule. Park [6] created nodules on a Zircaloy-4 clad tube in the lab conditions at 1000 °C. Trowse et al. [7] also studied the nodular corrosion in steam generating heavy water reactor conditions (SGHR), which is more relevant to the present work. Presence of nodular corrosion was reported on clad tubes and centre support tubes of SGHR with coolant pressure approximately equals to 7 MPa. They observed the nodules at reactor operating conditions at 282 °C and peak fuel rating upto 34 kW/m has been used, corresponding to surface heat flux of 69 W/cm$^2$. The peak fast neutron flux ( $>$ 1 MeV) at the fue cladding was 5.4 $\times$ 10$^{13}$ neutrons/cm$^2$ s. Clad tubes and centre support tubes were made of cold worked, stress relieved and recrystallized Zircaloy-2 material. Cross sectional optical image of the oxide nodule [7] is shown in Fig. 8. In order to calculate the bulging height of the nodule, a portion of nodular oxide is marked and a uniform oxide layer is removed from the total bulging height as shown in Fig. 8(b). So that the protrusion that occurred due to the nodule only is considered to compare with the experimental results.

The growth of oxide nodule of given size in Fig. 8(b) was simulated using the methodology described in section 2.2 with initial nuclei of size 100$\mu$m $\times$ 10$\mu$m, material property values of Zircaloy-2 were taken from Ref. [34] at operating temperatures and neutron fluence of SGHR and for Zirconium oxide material properties values were taken from Ref. [35]. Bulging height obtained by FEM simulation compared with the nodule grown in SGHR reactor as shown in Fig. 9. These results are observed to be in very good agreement with each other. The difference in the results obtained could be due to neglecting the curvature of tube and anisotropy in material behaviour.

### 2.5. Bulging height

The bulging heights of different nodules considered in this work are plotted as a functions of the aspect ratio of the nodules in Fig. 10. From the plot, it can be observed that the bulging height is almost independent of the aspect ratio and equals 40–45% of the depth of the nodule.

The bulging height is also calculated for hydride blister case by imposing a volumetric strain of 17.2% [13,36] and following the methodology described in section 2.2. Bulging height is independent of aspect ratio in case of hydride blister also. It is 11–12% of the depth of the hydride blister, which is very close to the values (10% of depth) in lab grown blisters by Puls [17].

## 3. Radial hydride formation

### 3.1. Modelling of radial hydride formation

Core components of PHWR, which are made of dilute zirconium alloys, pick up hydrogen during their service from corrosion reaction between the metal and the heavy water coolant. The nascent hydrogen released during the corrosion enters the zirconium as a solid solution. The maximum amount of hydrogen that remains in the solid solution without forming a precipitate is known as

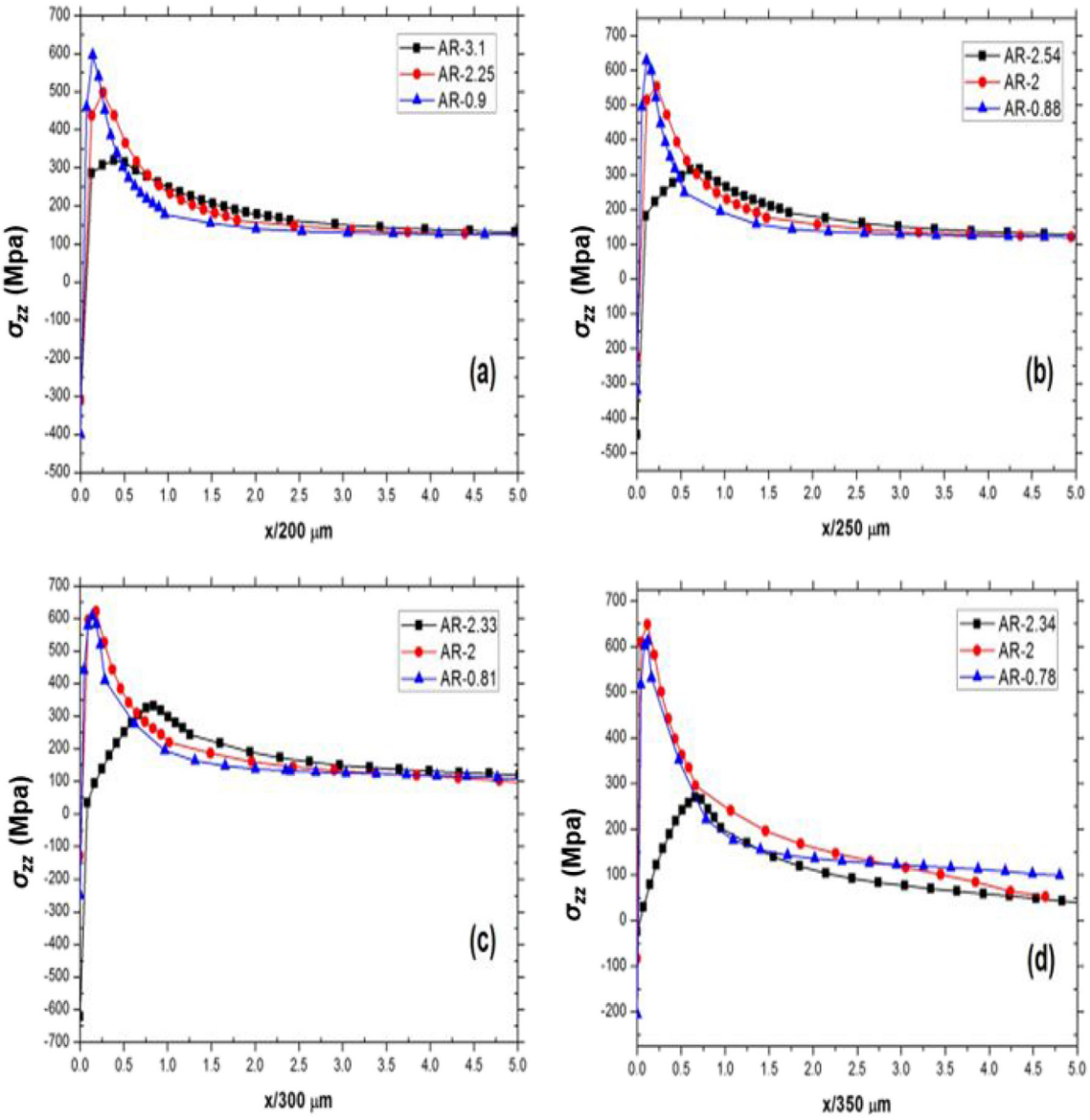


**Fig. 6.** Distribution of $\sigma_{zz}$ stresses for different aspect ratios ($AR$) as functions of a distance, normalised with respect to the depth of the nodule ($x/d$) ahead of its deepest point.

terminal solubility limit of precipitation (TSSP). Hydrogen in excess of the TSSP precipitates as hydrides in the zirconium matrix. The solubility limit was observed to increase with increase in temperature [36,37]. Therefore, when the temperature of the components is reduced to low from high temperature, hydrides are more likely to form at a given hydrogen concentration. Depending upon the cooling rate, hydrogen concentration and temperature, three types of hydrides can be formed in the dilute zirconium alloys [15]. They are $\gamma$-, $\delta$-, and $\varepsilon$-hydrides. However, due to cooling conditions possible under reactor operation, only $\delta$-hydride can form in the pressure tube material [15]. These hydrides tend to form in a platelet shape rather than in a needle shape. The hydride precipitation in Zr shows a habit plane parallel to the basal plane of the Zr [37–40]. The manufacturing routes of the PHWR pressure tube material is controlled in such way that it gives a desired texture. The crystallographic texture of the pressure tube material is such that around 43% of the basal poles are oriented in the radial direction of the tube, while 55% of the basal poles in are oriented in the circumferential direction and the remaining in the axial direction [41]. Hence, crystallographically there are two possible orientations for the hydrides in Zr 2.5% Nb PT material, they can form either in the circumferential or in the radial directions. The hydrides oriented in circumferential axial plane are called circumferential hydrides and hydrides oriented in radial axial plane are called radial hydrides. Predominantly these hydrides are observed to be formed at the grain boundaries and grows into the grains [42]. The $\alpha$-Zr grains of the pressure tube material are elongated in axial direction. The dimensions of the $\alpha$-Zr grains of Zr-2.5%Nb are in the ratio of 1:10:75 in the radial, circumferential and axial direction, respectively [41]. Therefore, for given volume of pressure tube material, Grain boundary area is more in circumferential axial plane compared to radial axial plane. Even though there are basal planes oriented along AR (Axial-Radial) plane, hydrides cannot be accommodated in AR plane. Hence, only circumferential hydrides form in the Zr-2.5%Nb PT material due to its microstructure. However, radial hydrides can be formed when the material is cooled under stress. This phenomenon of precipitation of radial hydrides under stress is called stress-reorientation of hydrides [15].

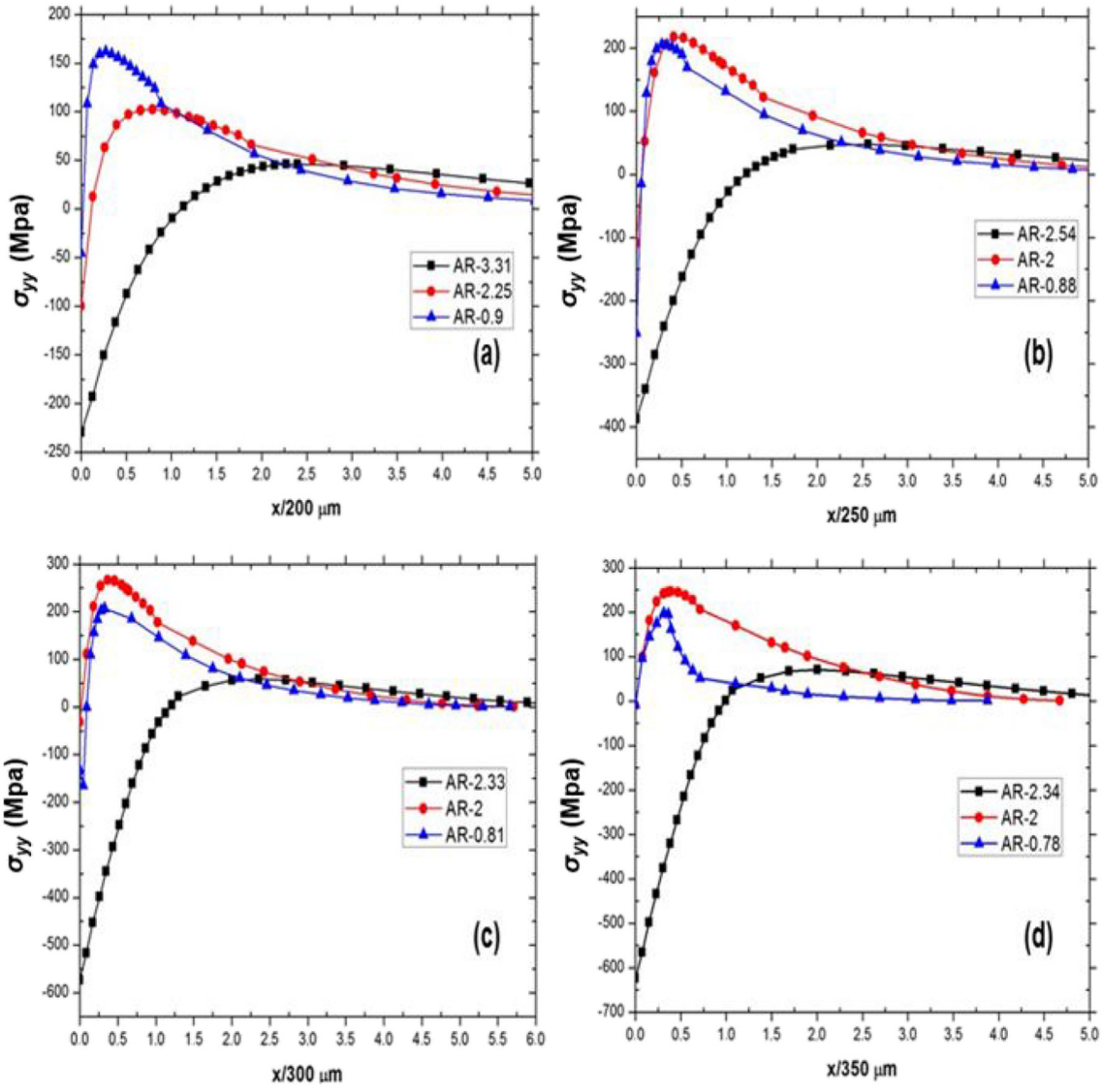


**Fig. 7.** Same as Fig. 6 for stresses $\sigma_{yy}$.

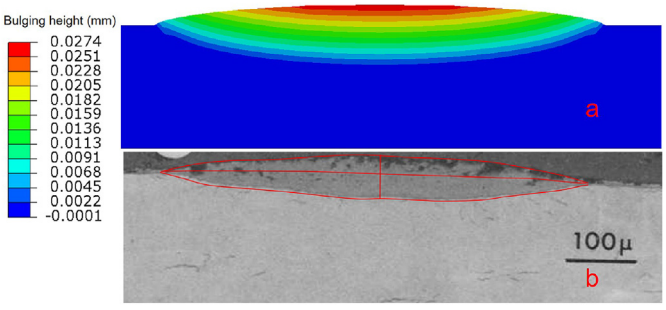


**Fig. 8.** Comparing the (a) contour plot of bulging height with (b) experimentally grown nodule in Zircaloy-2 [7].
Reprinted, with permission, from Zirconium in the Nuclear Industry, 1977, STP633, copyright ASTM International, 100 Barr Harbor Drive, West Conshohocken, PA 19428. EUR.

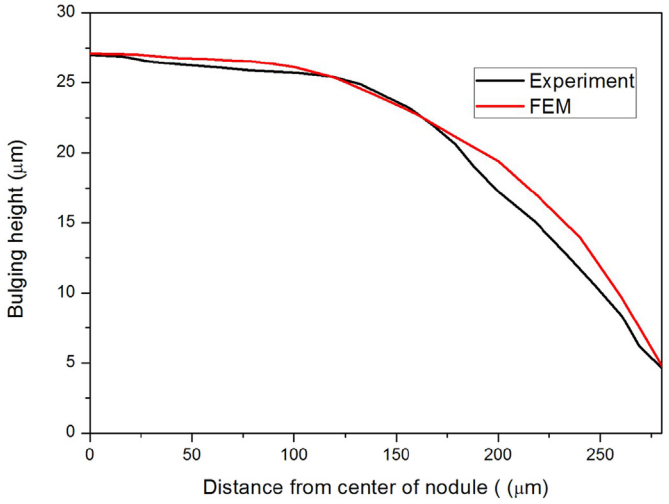


**Fig. 9.** Variation of bulging height from the centre of nodule to the periphery of the nodule.

The reorientation occurs above a certain threshold stress, $\sigma_{th}$. The reorientation stress was reported to depend on the temperature during cooling and material strength [26]. The threshold stresses

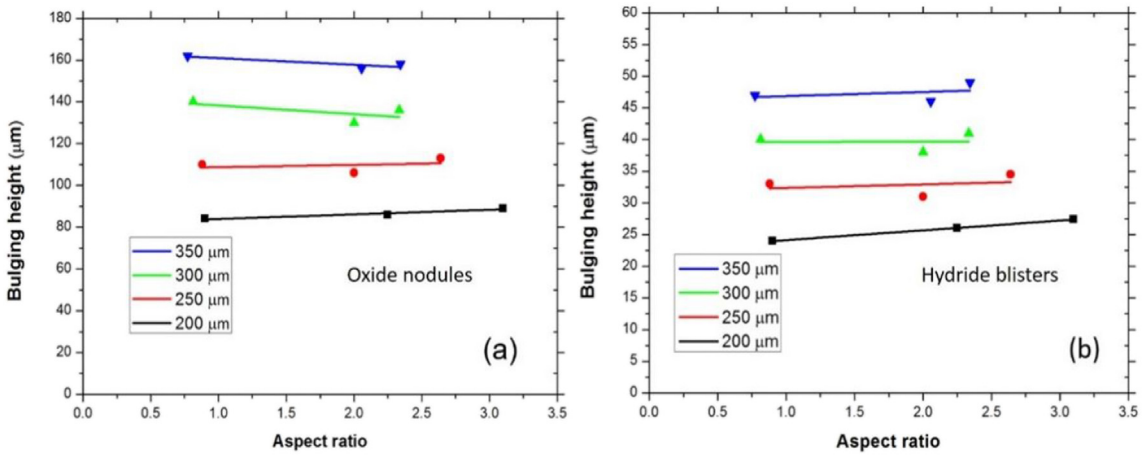


**Fig. 10.** Plot of maximum bulging height at centre of the (a) oxide nodule and (b) hydride blister as a function aspect ratio with different depths of the oxide nodule and hydride blister respectively.

were determined by applying a uniaxial stress. It has been found that $\sigma_{th}$ is around 180 MPa-200 MPa for Zr-2.5%Nb pressure tubes [43] at 573K. However, stress generated in the pressure tube near the oxide nodule due to its formation is multiaxial as discussed in section 2.3. Cinbiz et al. [44] concluded in their work, that the state of stress influences the hydride reorientation in zirconium alloys. The radial hydrides in the pressure tube end up with the formation of through thickness cracks by DHC mechanism as discussed. Crack growth by DHC occurs in three stages. Initially hydride nuclei will be formed. In the next stage hydride grows to a critical size and finally a crack is initiated including subsequent crack growth.

Puls [25] and Ells [22] based on their work concluded that preferential orientation of hydrides under stress is more pronounced in the nucleation stage. Therefore, the fraction of hydrides formed along any given plane depends on the number of favourable nuclei formed. Assuming that hydride formation is proportional to the number of nuclei, the rate of nucleation $N_i$, can be given by the following the expression [45].

$$N_i = \omega S_i \exp\left(-\frac{\Delta G_m + \Delta G^*}{kT}\right) \quad \left[\text{nuclei}/\text{m}^3/\text{s}\right], \tag{3}$$

where $\omega$ is a factor that depends on the vibration frequency of atoms and the area of the critical nucleus, $\Delta G_m$ is the activation energy for atomic migration and may be assumed to be independent of hydride orientation and temperature, $\Delta G^*$ is the activation energy barrier to nucleation, $S_i$ is the concentration of nucleation sites per unit volume for any given orientation, $k$ is the Boltzmann constant and $T$ is temperature in kelvin. For a any given temperature both $\omega$ and $\Delta G_m$ are assumed to be the same for both radial and circumferential hydride nuclei as they bear the same orientation relationship with the matrix. The activation barrier energy consist of three components, the chemical free energy to form critical nuclei from the solid solution ($\Delta G_c$), the interfacial free energy to form interface between the two phases i.e. matrix material and hydride ($\Delta G_i$), strain energy generated in the system during hydride formation ($\Delta G_s$),

$$\Delta G^* = -\Delta G_c + \Delta G_i + \Delta G_s. \tag{4}$$

The negative sign in the chemical potential energy indicates that $\Delta G_c$ reduces during the formation of hydride from the solid solution.

The strain energy term ($\Delta G_s$) contains two components, the accommodation energy per unit volume ($\Delta G_s^{acc}$) and the interaction energy per unit volume ($\Delta G_s^{int}$) [20,36]. Hence,

$$\Delta G_s = \Delta G_s^{acc} + \Delta G_s^{int}. \tag{5}$$

The accommodation energy is the energy generated in the hydride and the Zr-2.5%Nb matrix system upon phase transformation. It depends on size and shape of the formed hydride. The external work done on the Zr-H system in introducing hydrogen atoms in the Zr-2.5%Nb matrix material or hydride phase under stress is known as the interaction energy and is defined as follows [36],

$$\Delta G_s^{int} = pV_H x\,\delta n - \sigma_{ij}\,\varepsilon^T\,V_0 \tag{6}$$

where, $p$ is the hydrostatic stress, $V_H$ is the molal volume of hydrogen in the zirconium, $\delta n$ is the number moles of hydride. Assuming mole of hydride has composition $ZrH_x$ where $x = 1$ or 1.66. The applied stress field, $\sigma_{ij}$ and $\varepsilon^T$ is stress free transformation strain of zirconium hydride, $V_0$ is critical volume of hydride nuclei formed, due to uncertainty in exact value of the critical volume, its value is assumed to be $7.5 \times 10^{-27}\text{mm}^3$ for both radial and circumferential hydrides [23].

The number of nucleation sites $S_i$ for preferred hydride orientation is proportional to number of basal poles oriented in that direction, thus one can say that

$$S_i \propto f_n^i, \tag{7}$$

where $\propto$ denotes proportionality. The parameter $f_n^i$ is the fraction of basal poles along direction $i$.

As hydride nuclei formed is proportional to the area of grain boundaries in their respective direction.

$$\begin{aligned} S_i &\propto A_i, \quad (a) \\ S_i &\propto d_R d_A, \quad (b) \\ S_i &\propto d_C d_A, \quad (c) \end{aligned} \tag{8}$$

where $d_R$, $d_A$, $d_C$ are dimensions of the $\alpha$-Zr grain in the radial, axial, circumferential directions of the pressure tube, respectively.

Thus, using equation (3) by considering the appropriate parameters the ratio of nucleation rate for radial ($N_r$) and circumferential ($N_c$) hydrides can be written as:

$$\frac{N_r}{N_c} = \frac{S_r}{S_c}\exp\left(\frac{\Delta G^*_c - \Delta G^*_r}{xkT}\right), \quad (a),$$
$$\frac{N_r}{N_c} = \frac{S_r}{S_c}\exp\left(\frac{\Delta G^*_{c,acc} + \Delta G^*_{c,int} - \left(\Delta G^*_{r,acc} + \Delta G^*_{r,int}\right)}{xkT}\right), \quad (b), \tag{9}$$

where, $\Delta G^*_{,acc}$ is the accommodation energy of the hydride and $\Delta G^*_{,int}$ is the interaction energy of the hydride. The subscripts $r$ and $c$ refer to radial and circumferential hydrides, respectively. In view of the above discussion and by cancelling out the common terms Eq. (9) can be written,

$$\frac{N_r}{N_c} = \frac{f^r_n}{f^c_n}\frac{d_R}{d_c}\exp\left(\frac{\Delta G^*_{c,acc} - \Delta G^*_{r,acc} + \Delta G^*_{c,int} - \Delta G^*_{r,int}}{xkT}\right), \tag{10}$$

where the terms $\Delta G^*_{c,acc}$, $\Delta G^*_{r,acc}$ are accommodation energies for radial and circumferential hydrides, respectively and the terms $\Delta G^*_{c,int}$, $\Delta G^*_{r,int}$ are the interaction energy for radial and circumferential hydrides, respectively. Thus, the percentage of nucleation sites for radial hydride formation in a given volume is given as

$$\eta = \frac{N_r}{N_c + N_r}. \tag{11}$$

The energy density $\Delta G^*_{,acc}$ depends on the volume of the hydride formed. It does not depend on external stress applied and can therefore be calculated as described in the following subsection.

### 3.2. Accommodation energy of hydride platelet

A very small hydride plate is assumed to be formed inside the circular disk. The size of the simulated part of the disk is chosen to be one hundred times that of the hydride size in order to simulate the conditions of a large and virtually infinite matrix. An axisymmetric finite element model is used to calculate the stress and strains in the matrix and the hydride. The material properties of the Zr-2.5%Nb at 300 °C [28] are used and the zirconium hydride is assumed to have the same elastic modulus as that of the Zr-2.25% Nb matrix. Four node axisymmetric (CAX4R) elements with reduced integration are used for the calculations. The matrix material is transformed to hydride material by imposing a volumetric expansion strain of 17.2%. The strain energy of the model is calculated and normalised with the volume of the hydride. Its value is found to be 42.85 MJ/m$^3$.

It is well known that the grain boundaries are the heterogeneous sites for the nucleation of hydride precipitates [45]. The linear extent of the $\alpha$-Zr grain is very small in the radial direction compared with the axial direction and even if the radial hydride nuclei is formed it is difficult for the hydrides to grow into other grains because the grains are usually not well aligned. Hence, circumferential hydrides are assumed to be formed on the grain boundaries while radial hydrides are assumed to be formed within the grains. The accommodation energy is supposedly less for the circumferential hydrides. Moreover, the reduction of accommodation energy depends on the grain boundary packing density. The difference in packing density is suggested to be one percent by Ref. [46]. Thus, out of the around 17% misfit strain of the $\delta$-hydride with respect to the $\alpha$-phase, only about 16% need to be accommodated if the hydride nuclei forms within the grain boundary. Assuming accommodation energy of the precipitate is proportional to the square of the stress-free transformation strain. We can write

$$\frac{\Delta G^*_{c,acc}}{\Delta G^*_{r,acc}} = \left(\frac{\varepsilon^T_{gb}}{\varepsilon^T}\right)^2, \tag{12}$$

where, $\varepsilon^T = \varepsilon_1 + \varepsilon_2 + \varepsilon_3$ which represents the principal stress free transformation strain with respect to $\alpha$-phase and $\varepsilon^T_{gb}$ is the stress free transformation strain with respect to the grain-boundaries.

To calculate the interaction energy per unit volume, one need the stress free transformation strains of the hydrides with respect to the $\alpha$-Zr matrix. These values also depend on the temperature and given in literature [13]. The principal misfit strains of the hydrides at 573K are given as follows,

$$\varepsilon^T_{c,1} = \varepsilon^T_{c,2} = \varepsilon^T_{r,1} = \varepsilon^T_{r,3} = 0.052, \text{ and } \varepsilon^T_{c,3} = \varepsilon^T_{r,2} = 0.078\,. \tag{13}$$

The interaction energy of hydride can be calculated by putting these strains and computed stresses into Eq. (9). Once the interaction energy is calculated and $\Delta G^*_{,acc}$ are obtained, the fraction of radial nuclei hydride can be computed from Eq. (11).

### 3.3. Application to hydride blister in Zr-2.5%Nb

The hydride model is applied to the hydride blister for validation and compared with the experimentally grown blisters [5]. An initial hydride nuclei with depth of 50$\mu$m and a largest radius 1 mm is assumed to be formed. The growth of the hydride is modelled as described for the oxide nodule in section 2.2. The final hydride blister modelled is compared with a cut through experimentally grown hydride blister [5] shown in Fig. 11.

After the size of the hydride blister has been obtained in the analysis, the resulting stress field due to its growth is given as input to the reorientation model to calculate the percentage of the radial hydride nuclei formed in the Zr −2.5%Nb PT matrix material. The contour plot of the fraction of radial hydride nuclei ($\eta$) is shown in Fig. 12. It is observed to be matching well with the experimental results.

### 3.4. Application to oxide nodule in Zr-2.5%Nb

The hydride reorientation model described above is also applied to oxide nodule cases in the Zr-2.5%Nb pressure tube material at 573K. Different sizes of the oxide nodules are modelled and the stress fields due to their growth obtained along with the stresses caused by internal pressure in the pressure tube. The FEM output of normal stress components in the Zr-2.5%Nb material is used to calculate the radial hydride nuclei fractions. The ratio of total volume of the matrix containing more than 50% radial hydrides to the volume of oxide nodule or hydride blister is represented by parameter $k$. The plot of $k$ versus the aspect ratio for different depths of blisters or nodules is shown in Fig. 13. The plot suggests that the region of radial hydride formation depends on type of precipitate formed and also on the aspect ratio of the precipitate.

The plot in Fig. 13 suggests that for lower aspect ratios nearly similar values of parameter $k$ is obtained for oxide nodules and hydride blisters despite oxide nodules being associated with large transformation strain as compared to hydride blisters. The effect of difference in transformation strain between oxide nodule and hydride blister is evident only at large aspect ratios. For the multi axial stress state the fraction of radial hydride is not expected to depend on the absolute value of the stresses rather it depends on the difference between $\sigma_{zz}$ and $\sigma_{yy}$ as is explained in section 3.1. Therefore, $(\sigma_{zz} - \sigma_{yy})$ is plotted as functions of normalised distance along the thickness direction of the model for both hydride blister and oxide nodule cases as shown in Fig. 14. Curves with square symbols

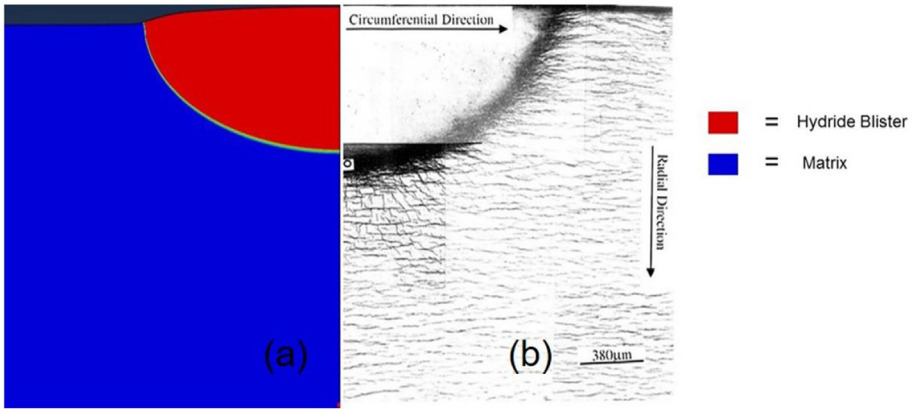


**Fig. 11.** Comparing the modelling result with an experimentally grown hydride blister.

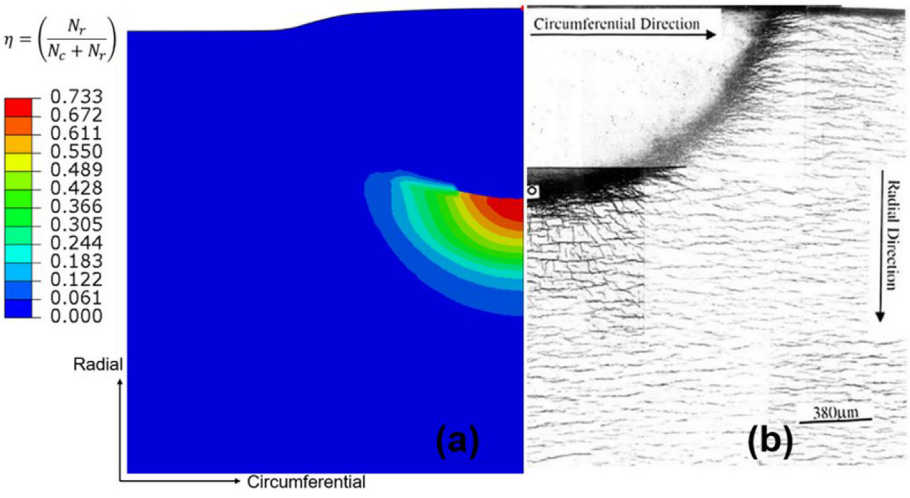


**Fig. 12.** (a) Contour plot of the fraction of radial hydride nuclei $\eta$, (b) radial hydrides below the hydride blisters.

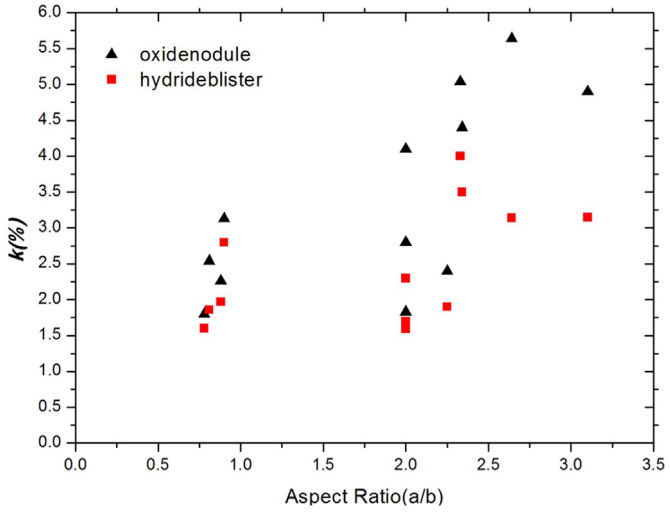


**Fig. 13.** Variation of $k(\eta > 0.5)$ with the aspect ratio $(a/b)$.

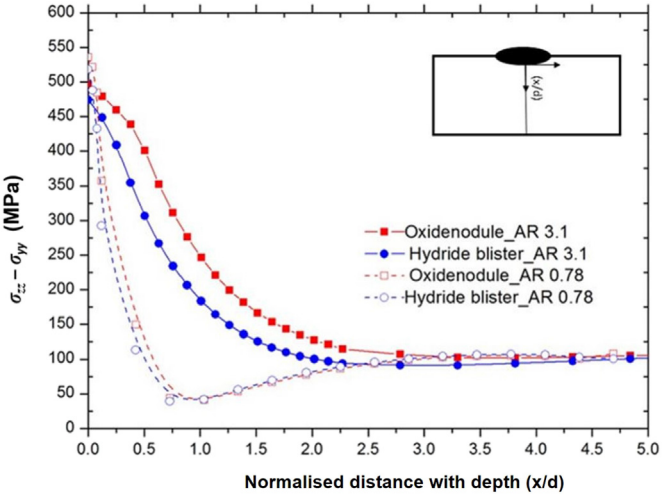


**Fig. 14.** Plot of the variation of $\sigma_{zz} - \sigma_{yy}$ with the normalised distance with the depth $x/d$.

represent the oxide nodule results whereas those with circle symbols represent the hydride blister results. It is observed from the plot that $(\sigma_{zz} - \sigma_{yy})$ is nearly the same for both oxide nodules and hydride blisters in cases of small aspect ratios. In the cases of larger aspect ratios, the difference in stress is more for oxide nodule. Hence, value of $k$ is more in the oxide nodule case as compared to the hydride blister for larger aspect ratios.

## 4. Stress intensity factors calculation

It is observed from the above results that the stress field generated during the growth of the oxide nodules along with the externally applied stress is sufficient to create radial hydrides below the nodule by the stress reorientation phenomenon. The computation done in the above sections does not include cracks. Although the computed stress fields give quantitative values of stresses in all direction and size of nodules, which are critical for DHC initiation qualitatively, it is not possible to determine size of the critical nodules quantitatively. In literature, reporting experimental results concerning DHC, a fatigue pre-crack is usually used [47,48]. Through the tests a threshold stress intensity factors have been determined [37,39,46,47].

Shi and Puls [52] reported that the fracture stress of an embedded hydride decreases with increase in hydride plate length and for hydride plate lengths greater than 50$\mu$m the stress is around 600 MPa and is independent of the length of the hydride. Thus, the region below the nodule in which the stress values are greater than 600 MPa as described in section 2, hydrides of length greater than 50$\mu$m may fracture. From the reorientation experiments conducted by Singh et al. [26] the critical size of single radial hydrides is about 50$\mu$m. Single radial hydrides with a depth of 50$\mu$m in radial direction and 100$\mu$m in axial direction are assumed to fracture. Therefore, a predefined planar crack of size 50$\mu$m $\times$ 100$\mu$m in the axial radial plane at the deepest point of the nodule is defined as shown in Fig. 3. The crack is normal to the applied hoop stress. With this predefined crack, the methodology described in section 2.2 is followed to obtain the stresses surrounding the hydride.

To capture the stress singularities at the crack faces, a fine mesh must be used or special elements like node collapsed elements must be used. As the element size used in this analysis is already small, it seems ideal to use the former method. However, usage of elements with specific shape functions able to handle displacement discontinuities have been included in several FEM-codes such as the presently used. The tool, called XFEM, is based on the FEM technique that is especially designed for treating the discontinuities without mesh complexities and facilitates the user implementation [49–51].

The XFEM enrichment for the predefined crack was used at the deepest point of the oxide nodules, which were previously grown to a final size by using the methodology described in section 2.2. The energy release rate is calculated for different oxide nodules by using the *J*-integral approach. The potential stress intensity factor, $K_J$, was calculated by using the following plane strain expression.

$$K_J = \sqrt{\frac{JE}{1-\nu^2}}. \tag{14}$$

Plane stress gives a 9% higher $K_J$. The plain strain condition is used here as it is believed that this is closer to reality as the crack is embedded in the Zr-2.5%Nb matrix. The calculated values of are plotted for different size of the oxide nodules. From Fig. 15 (a), it is observed that values are decreasing mildly with the increase in the aspect ratio of the nodule up to the value of two. Thereafter, values are decreasing very sharply. As the aspect ratio is increasing for given depth of the nodule, constraint to grow is decreasing, thereby the reducing the stresses. Hence, values are reducing. For a given aspect ratio, values are increasing with increase in depth of the nodule. With increase in depth of the nodule the constraint offered by matrix is increasing and it is more like deeper crack. Thus, stresses generated are increasing, which will indeed increase the values. The threshold stress intensity factor ($K_{IH}$) depends on the radial basal pole fraction in the matrix material and manufacturing routes [16,46,47], and typical values for unirradiated pressure tube material are reported to be between 8.5 and 10.5 MPa$\sqrt{\text{m}}$. To be on the conservative side, one may take the lower value $K_{IH}$ = 8.5MPa$\sqrt{\text{m}}$ for unirradiated materials, then nodules having aspect ratio less than 2 and a depth more than 350 $\mu$m may initiate crack growth DHC as shown in Fig. 15(a). Of course this requires that the crack region is supplied with sufficient amounts of hydrogen.

### 4.1. Effect of irradiation

To investigate the effect of irradiation on $K_J$, the yield strength of the material increased by 60% and ductility of the material decreased by 70% [24]. With these material behaviour inputs, the computations are performed for different sizes of oxide nodules. The calculated values of the $K_J$ are plotted in Fig. 15(b). From the plot, it is observed that $K_J$ is the same as for the unirradiated material for shallow nodules. But as the aspect ratio is decreasing, $K_J$ exhibit a strong dependence of nodule depth. To understand this difference, the distribution of stress components $\sigma_{yy}$ and $\sigma_{zz}$ ahead of the oxide nodule in the matrix material are plotted in Fig. 16. As observed, the stress distribution is the same for both unirradiated and irradiated materials for the oxide nodules having aspect ratios of 0.78–3. The irradiation decreases the $K_{IH}$ value according to Sagat et al. [53]. Therefore, if one considers the lower bound $K_{IH}$ value for irradiated material as 4.5 MPa$\sqrt{\text{m}}$, then the nodules, which are having aspect ratios less than 2.5 and depth more than 200 $\mu$m can initiate DHC in the matrix as is observed in Fig. 15(b) provided that a sufficient amount of hydrogen is present. The results that are based on estimated material properties may have to be adjusted when new data is available.

### 4.2. Pressure tube failure mode

In the forgoing, the mechanics of events such as hydride blister or oxide nodule formation, formation of radial hydrides, and their fracture and crack growth through DHC are described. The growth of the hydride blister or oxide nodule to a certain depth at which stable crack growth through DHC mechanism can take place is required. The growth may continue till a part of the remaining ligament of the pressure tube is unable to support the internal pressure. It is reported that the initial crack growth velocity due to DHC along axial direction is about 2–3 times of that along radial direction [54]. Thus, even to start with if a crack originating from hydride blister or oxide nodule is of semi-circular shape once the crack growth through DHC has started it will acquire semi-ellipsoidal shape with aspect ratio of 2–3. If the critical crack length (CCL) of the material is more than five times the wall thickness Leak Before Break (LBB) is likely to occur [55].

The CCL values of Zr-2.5%Nb alloy pressure tube material depends on the temperature, hydrogen content and hydride orientation [56]. The values of CCL for Zr-2.5Nb pressure tubes manufactured from quadruple melted ingots is reported to be greater than 70 mm under reactor operating condition and reduces to 50 mm for the material containing 100 wppm hydrogen with hydrides having circumferential orientation. The CCL value for the material containing 100 wppm of hydrogen with hydrides having radial orientation is reduced to less than 20 mm below 250 °C. For leak before break to occur the flaw size due to nodule formation and its growth because of DHC must be greater than 5*t*, where *t* is the wall thickness of the tube, before it becomes through thickness. Thus for pressure tubes containing up to 100 wppm hydrogen with hydrides being circumferentially oriented LBB criteria will be satisfied. However, if the hydrides are radially oriented, LBB may not be satisfied and in such a situation break before leak may occur.

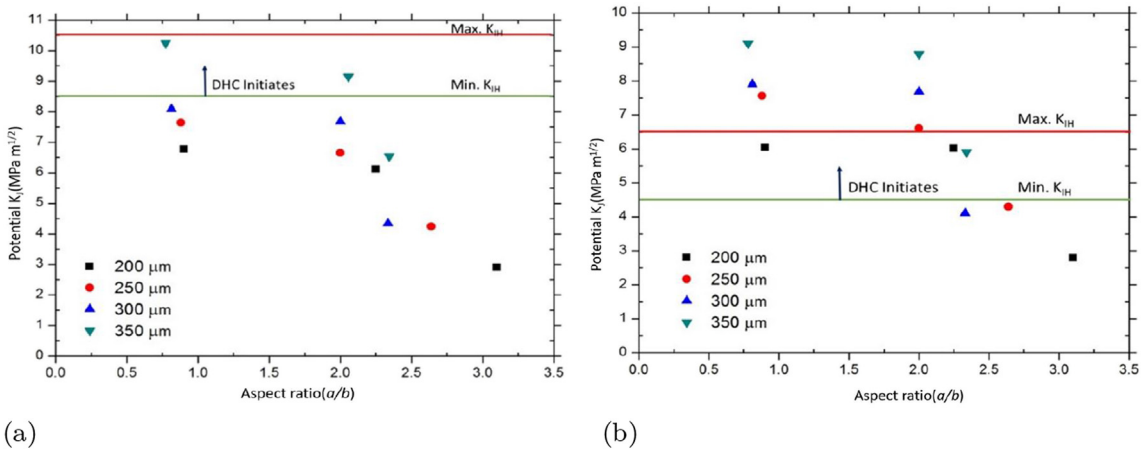


**Figure 15.** Variation of $K_J$ as a function of the aspect ratio of the oxide nodule with different depths of the oxide nodule in (a) unirradiated and (b) irradiated Zr-2.5%Nb.

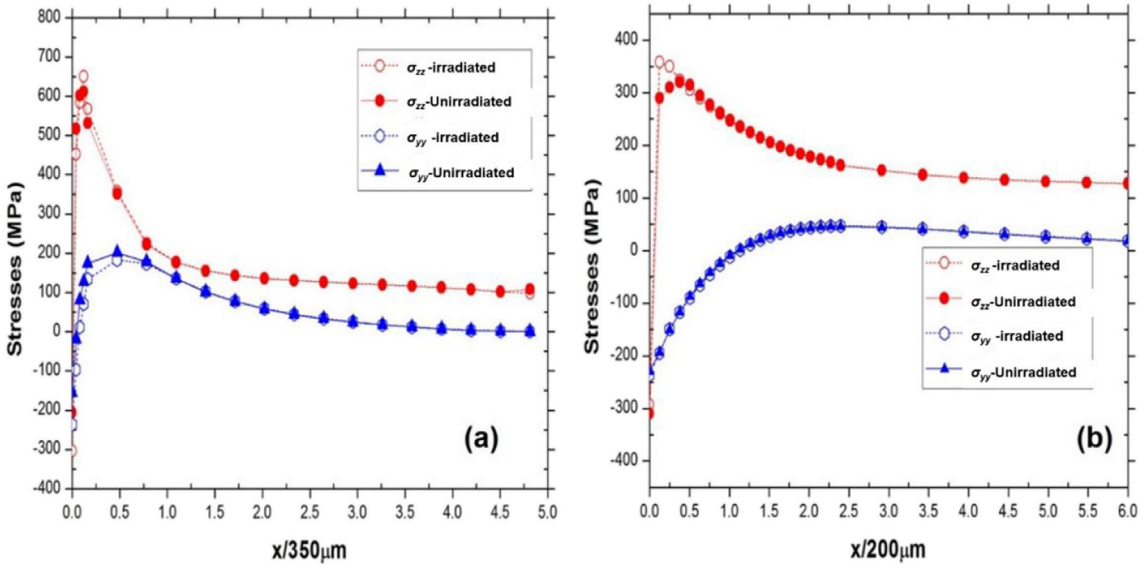


**Figure 16.** Distribution of stresses ahead of deepest point of oxide nodule as function of normalised distance ($x/d$) for (a) aspect ratio 0.78 and (b) aspect ratio 3.1.

## 5. Summary and conclusions

The formation of the oxide nodule is simulated in Zr-2.5Nb alloy pressure tube material using a finite element method. Incremental growth of the nodule was modelled to identify the region in which radial hydride will form, to determine the hydride plate that is likely to crack and to predict the nodule depth for which crack growth in the matrix through DHC will occur. The simulation methodology is validated by comparing the bulge height of the hydride blister formed in Zircaloy, which was found to be in good agreement.

Before the introduction of the crack, the model has only one single length scale, the linear size of the hydride. This implies that the geometry should be self similar and independent of the amount of blister or nodule size. This is also supported by the observations. The bulge height is consequently proportional to the bulge depth and independent of Aspect-Ratio(AR). In cases for oxide nodules, about 41–42% of the depth of the nodule and in cases for hydride blisters, about 11–12% of depth of the blister.

The stress state in nodule region is very complex. Top layers of the nodule experience high tensile stress, thereby microcracks are expected to form in the top layers of the oxide nodule. The stresses in the matrix are observed to be decreasing with increasing aspect ratio of the nodule, therefore deeper nodules are more detrimental compared to the shallower nodules. The stresses are decaying as one move away from the matrix/nodule interface. The pronounced effect of the oxide nodule is up to a distance of about four times the depth of the nodule in the matrix material.

A new model for prediction of radial hydride formation under the given stress field by considering grain size and shape, texture and state of stress is proposed and validated with the radial hydrides formed below the lab grown hydride blister. The volume of radial hydrides formed is the same for both hydride blisters and oxide nodules in cases of smaller aspect ratios, but it is larger for oxide nodules having a larger aspect ratio.

The XFEM computations are performed to calculate the potential stress intensity factors of the oxide nodules. Irradiation effects are also simulated by increasing the material yield strength and decreasing the ductility. In cases of unirradiated matrix material, oxide nodules having aspect ratios less than two and depths more than 350 $\mu$m can initiate DHC. In cases of irradiated matrix material, nodules having aspect ratios less than 2.5 and depths more than

200 $\mu$m can initiate DHC in matrices. If the crack or flaw from nodule attained due to DHC is less than critical crack length (CCL), before it reaches through thickness, Leak Before Break occurs. Otherwise, Break Before Leak will occur.

## Acknowledgements

Constant encouragement and support provided by Dr. G. K. Dey, former Director, Materials Group and Dr. K. Madangopal, AD Materials Group, BARC Dr. D. Srivastava, Chief Executive, NFC Hyderabad and Mr. U. C. Muktibodh, Former Director (T) and Mr. A.K. Balasubrahmanian Director(T) NPCIL are acknowledged. Thanks goes to Dr. Arpan Das, Dr. Abhishek Tiwari, Mr. Saurav Sunil and Mr. Avinash Gopalan of MMD and Dr. Naveen Kumar N. of Materials Science Division for fruitful discussions.

## Appendix A. Supplementary data

Supplementary data to this article can be found online at https://doi.org/10.1016/j.jnucmat.2018.10.040.

## References

[1] J.D. Eshelby, The determination of the elastic field of an ellipsoidal inclusion, and related problems, Proc. Roy. Soc. Lond. Math. Phys. Sci. 241 (1226) (1957) 376–396.
[2] A.G. Khachaturyan, Elastic strain caused by crystal lattice rearrangement, in: Theory of Structural Transformations in Solids, John Wiley & Sons, New York, 1983, pp. 281–304.
[3] G. Field, J. Dunn, B. Cheadle, Analysis of the pressure tube failure at pickering NGS "A" unit 2 nuclear systems department, Canadian Metallurgical Quarterly 24 (3) (1985) 181–188.
[4] A. Sawatzky, Formation of hydride blisters in zirconium alloy pressure tubes, Canadian Metallurgical Quarterly 24 (3) (1985) 227–234.
[5] R.N. Singh, R. Kishore, T.K. Sinha, B.K. Kashyap, Hydride blister formation in Zr-2.5 wt% Nb pressure tube alloy, J. Nucl. Mater. 301 (2) (2002) 153–164.
[6] D.J. Park, J.Y. Park, Quantitative measurement of displacement and strain fields in the ZrO 2 layer during the transition to nodular oxidation, Corrosion Sci. 69 (2013) 61–66.
[7] F. Trowse, R. Sumerling, A. Garlick, Nodular Corrosion of Zircaloy-2 and Some Other Zirconium Alloys in Steam Generating Heavy Water Reactors and Related Environments, Zirconium in the Nuclear Industry, ASTM International, 1977.
[8] A.B. Johnason, Effects of Nuclear Radiation on the Corrosion, Hydriding, and Oxide Properties of Six Zirconium Alloys, Applications-related Phenomena in Zirconium and its AlloysEffects of Nuclear Radiation on the Corrosion, Hydriding, and Oxide Properties of Six Zirconium Alloys, Applications-related Phenomena in Zirconium and its Alloys, ASTM International, West Conshohocken, PA, USA, 1969, pp. 301–324. STP458-E8.
[9] V. Urbanic, The occurrence of ZrO2 wedging in cracked Zr-2.5 Wt% Nb alloy, Corrosion 33 (5) (1977) 188–190.
[10] C. Coleman, Effect of texture on hydride reorientation and delayed hydrogen cracking in cold-worked Zr-2.5 Nb, in: D.G. Franklin (Ed.), Zirconium in the Nuclear Industry, ASTM Int., West Conshohocken, PA, USA, 1982. STP754 10: 0803107544.
[11] E. Ibrahim, B. Cheadle, Development of zirconium alloys for pressure tubes in CANDU reactors, Canadian Metallurgical Quarterly 24 (3) (1985) 273–281.
[12] C. Williams, Development potential of zirconium alloys for high-temperature applications, React. Technol. 13 (1970) 147–169.
[13] R.N. Singh, P. Ståhle, A.R. Massih, A. Shmakov, Temperature dependence of misfit strains of $\delta$-hydrides of zirconium, J. Alloy. Comp. 436 (1) (2007) 150–154.
[14] R. Bedworth, N. Pilling, The oxidation of metals at high temperatures, J. Inst. Met. 29 (3) (1923) 529–582.
[15] D. Northwood, U. Kosasih, Hydrides and delayed hydrogen cracking in zirconium and its alloys, Int. Met. Rev. 28 (1) (1983) 92–121.
[16] R.N. Singh, N. Kumar, R. Kishore, S. Roychaudhury, T.K. Sinha, B.P. Kashyap, Delayed hydride cracking in Zr-2.5 Nb pressure tube material, J. Nucl. Mater. 304 (2) (2002) 189–203.
[17] M.P. Puls, Determination of fracture initiation in hydride blisters using acoustic emission, Metall. Mater. Trans. 19 (9) (1988) 2247–2257.
[18] Y.J. Kim, M.L. Vanderglas, Elastic-plastic analysis of hydride blisters in Zircaloy-2 pressure tubes, J. Pressure Vessel Technol. 110 (3) (1988) 276–282.
[19] M.L. Vanderglas, Y.J. Kim, Stresses due to volumetric expansion of zirconium hydride inclusions, Int. J. Pres. Ves. Pip. 22 (3) (1986) 177–196.
[20] R.N. Singh, J.K. Chakravartty, P. Ståhle, K. Sairam, B.P. Kashyap, Stress-field Computation for hydride blister forming in Zr-alloys, in: Water Reactor Fuel Performance Meeting-WRFPM2008, Korea, 2008.
[21] W. Reheman, P. Ståhle, E. Durgé, R.N. Singh, Phase field modelling of formation and fracture of expanding precipitates, Procedia Structural Integrity 3 (2017) 477–483.
[22] C. Ells, The stress orientation of hydride in zirconium alloys, J. Nucl. Mater. 35 (3) (1970) 306–315.
[23] D. Hardie, M. Shanahan, Stress reorientation of hydrides in zirconium-2.5% niobium, J. Nucl. Mater. 55 (1) (1975) 1–13.
[24] C. Silva, K. Leonard, M. Trammel, C. Bryan, Characterization of different forms of Zr-2.5 Nb samples before and after neutron irradiation, Mater. Sci. Eng. 716 (2018) 296–307.
[25] M.P. Puls, Hydrogen-induced Delayed Cracking-2, Effect of Stress on Nucleation, Growth and Coarsening of Zirconium Hydride Precipitates, Atomic Energy of Canada Limited, 1984, 8381.
[26] R.N. Singh, R. Kishore, S.S. Singh, T.K. Sinha, B.P. Kashyap, Stress-reorientation of hydrides and hydride embrittlement of Zr-2.5 wt% Nb pressure tube alloy, J. Nucl. Mater. 325 (1) (2004) 26–33.
[27] S. Bajaj, A. Gore, The indian PHWR, Nucl. Eng. Des. 236 (7) (2006) 701–722.
[28] R.N. Singh, S. Mukherjee, R. Kishore, B.P. Kashyap, Flow behaviour of a modified Zr-2.5 wt% Nb pressure tube alloy, J. Nucl. Mater. 345 (2) (2005) 146–161.
[29] Karlsson Hibbit, Sorensen, ABAQUS/Standard Analysis User's Manual, Hibbit, Karlsson, Sorensen Inc., USA, 2007.
[30] Azomaterials, Zirconia - $ZrO_2$, zirconium dioxide. https://www.azom.com/properties.aspx?ArticleID=133. (Accessed 21 June 2018).
[31] R.N. Singh, R. Kishore, T.K. Sinha, S. Banerjee, B.P. Kashyap, Stress field estimation around a semi-constrained inclusion and its validation by interpreting hydride platelet orientation around a blister in a Zr-2.5 Nb alloy, Mater. Sci. Eng. 339 (1) (2003) 17–28.
[32] P. Ståhle, R.N. Singh, S. Banerjee, Spontaneous fracture of growing precipitates with large misfit strain, Int. J. Fract. 165 (2) (2010) 189–197.
[33] B.W. Leitch, M.P. Puls, Finite element calculations of the accommodation energy of a misfitting precipitate in an elastic-plastic matrix, Metallurgical Transactions A 23 (3) (1992) 797–806.
[34] G.F. Rieger, D. Lee, Strength and ductility of neutron irradiatedand textured zircaloy-2, zirconium in nuclear applications, ASTM STP 551 (1974) 355–369.
[35] E. Sánchez-González, J.J. Meléndez-Martínez, A. Pajares, P. Miranda, F. Guiberteau, B.R. Lawn, Application of Hertzian tests to measure stress-strain characteristics of ceramics at elevated temperatures, J. Am. Ceram. Soc. 90 (1) (2007) 149–153.
[36] M.P. Puls, The effects of misfit and external stresses on terminal solid solubility in hydride-forming metals, Acta Metall. 29 (12) (1981) 1961–1968.
[37] R.N. Singh, S. Mukherjee, A. Gupta, S. Banerjee, Terminal solid solubility of hydrogen in Zr-alloy pressure tube materials, J. Alloy. Comp. 389 (1) (2005) 102–112.
[38] R.N. Singh, P. Ståhle, J.K. Chakravartty, A. Shmakov, Threshold stress intensity factor for delayed hydride cracking in Zr-2.5% Nb pressure tube alloy, Mater. Sci. Eng. 523 (1–2) (2009) 112–117.
[39] Y.S. Kim, S.S. Park, S.I. Kwun, Threshold stress intensity factor, KIH for delayed hydride cracking of a Zr-2.5 Nb tube with loading mode, J. Alloy. Comp. 462 (1–2) (2008) 367–375.
[40] D. Westlake, The habit planes of zirconium hydride in zirconium and zircaloy, J. Nucl. Mater. 26 (2) (1968) 208–216.
[41] D. Srivastava, G.K. Dey, S. Banerjee, Evolution of microstructure during fabrication of Zr-2.5 Wt pct Nb alloy pressure tubes, Metall. Mater. Trans. 26 (10) (1995) 2707–2718.
[42] K.M. Krishna, A. Sain, I. Samajdar, G.K. Dey, D. Srivastava, S. Neogy, R. Tewari, S. Banerjee, Resistance to hydride formation in zirconium: an emerging possibility, Acta Mater. 54 (18) (2006) 4665–4675.
[43] R.N. Singh, R.L. Mikin, G.K. Dey, D. Sah, I. Batra, P. Ståhle, Influence of temperature on threshold stress for reorientation of hydrides and residual stress variation across thickness of Zr-2.5 Nb alloy pressure tube, J. Nucl. Mater. 359 (3) (2006) 208–219.
[44] M.N. Cinbiz, D.A. Koss, A.T. Motta, The influence of stress state on the reorientation of hydrides in a zirconium alloy, J. Nucl. Mater. 477 (2016) 157–164.
[45] D.A. Porter, K.E. Easterling, M. Sherif, Phase Transformations in Metals and Alloys, (Revised Reprint), CRC press, 2009.
[46] R.N. Singh, P. Ståhle, T. Sathish, G.K. Dey, Modeling of temperature dependence of stress-reorientation of hydrides in CWSR Zr-alloys, in: Water Reactor Fuel Performance Meeting-WRFPM2008,Korea, 2008.
[47] S. Sunil, A. Bind, H. Khandelwal, R.N. Singh, J.K. Chakravartty, Delayed hydride cracking behavior of Zr-2.5 Nb alloy pressure tubes for PHWR700, J. Nucl. Mater. 466 (2015) 208–219.
[48] Y. Kim, Y.G. Matvienko, Y. Cheong, S. Kim, S. Kwon, A model of the threshold stress intensity factor, K IH, for delayed hydride cracking of Zr-2.5 Nb alloy, J. Nucl. Mater. 278 (2) (2000) 251–257.
[49] T. Belytschko, T. Black, Elastic crack growth in finite elements with minimal remeshing, Int. J. Numer. Methods Eng. 45 (5) (1999) 601–620.
[50] N. Moës, J. Dolbow, T. Belytschko, A finite element method for crack growth without remeshing, Int. J. Numer. Methods Eng. 46 (1) (1999) 131–150.
[51] T.P. Fries, T. Belytschko, The extended/generalized finite element method: an overview of the method and its applications, Int. J. Numer. Methods Eng. 84 (3) (2010) 253–304.
[52] S.-Q. Shi, M.P. Puls, Fracture strength of hydride precipitates in Zr-2.5 Nb alloys, J. Nucl. Mater. 275 (3) (1999) 312–317.
[53] S. Sagat, C.E. Coleman, M. Griffiths, B.J. Wilkins, The effect of fluence and

irradiation temperature on delayed hydride cracking in Zr-2.5 Nb, in: Zirconium in the Nuclear Industry: Tenth International Symposium, ASTM International, 1994.
[54] Y.S. Kim, Y.M. Cheong, Anisotropic delayed hydride cracking velocity of CANDU Zr-2.5 Nb pressure tubes, J. Nucl. Mater. 373 (1) (2008) 179–185.
[55] G. Moan, C. Coleman, E. Price, D. Rodgers, S. Sagat, Leak-before-break in the pressure tubes of CANDU reactors, Int. J. Pres. Ves. Pip. 43 (1–3) (1990) 1–21.
[56] R.K. Sharma, A. Bind, G. Avinash, R.N. Singh, A. Tewari, B. Kashyap, Effect of radial hydride fraction on fracture toughness of CWSR Zr-2.5% Nb pressure tube material between ambient and 300°C temperatures, J. Nucl. Mater. 508 (2018) 546–555.